NANO · MICRO small
www.small-journal.com

Large-Scale Growth and Field-Effect Transistors Electrical Engineering of Atomic-Layer SnS_2

Liping Xu, Peng Zhang, Huaning Jiang, Xiang Wang, Fangfang Chen, Zhigao Hu, Yongji Gong,* Liyan Shang, Jinzhong Zhang, Kai Jiang, and Junhao Chu*

2D layers of metal dichalcogenides are of considerable interest for high-performance electronic devices for their unique electronic properties and atomically thin geometry. 2D SnS_2 nanosheets with a bandgap of ≈2.6 eV have been attracting intensive attention as one potential candidate for modern electrocatalysis, electronic, and/or optoelectronic fields. However, the controllable growth of large-size and high-quality SnS_2 atomic layers still remains a challenge. Herein, a salt-assisted chemical vapor deposition method is provided to synthesize atomic-layer SnS_2 with a large crystal size up to 410 µm and good uniformity. Particularly, the as-fabricated SnS_2 nanosheet-based field-effect transistors (FETs) show high mobility (2.58 $cm^2 V^{-1} s^{-1}$) and high on/off ratio (≈10^8), which is superior to other reported SnS_2-based FETs. Additionally, the effects of temperature on the electrical properties are systematically investigated. It is shown that the scattering mechanism transforms from charged impurities scattering to electron–phonon scattering with the temperature. Moreover, SnS_2 can serve as an ideal material for energy storage and catalyst support. The high performance together with controllable growth of SnS_2 endow it with great potential for future applications in electrocatalysis, electronics, and optoelectronics.

1. Introduction

Recently, 2D semiconductor materials with lamellar structures have emerged as a promising candidate for a replacement and/or complement to silicon. Transition metal dichalcogenides (TMDs) are the most known 2D semiconductors with the chemical formula MX_2, consisting of an atomic plane of a transition metal (M = Mo, W, Re, Sn, and so on) sandwiched between two chalcogen atomic planes (X = S, Se, Te).[1] 2D TMDs show a wide range of electronic, optical, chemical, and thermal properties that have attracted great attention because of their potential applications, such as electronics, optics, and catalysis.[2–18] Among them, MoS_2 has been the most widely studied one, which has an indirect bandgap of 1.29 eV in the bulk form, but interestingly, undergoes a transition toward a direct bandgap of 1.9 eV in the form of a single atomic layer.[19,20] While MoS_2 has shown its great significance for fundamental research and various applications, other TMDs may provide important access to new physics or novel devices as well.[21–25]

As one of the promising materials, 2D SnS_2 is an environment-friendly and earth abundant semiconductor material, which makes it as an important building block for sustainable clean energy electrocatalysis, electronic, and optoelectronic applications.[26] SnS_2 has an indirect bandgap of 2.08–2.44 eV, high optical absorption coefficient exceeding 10^4 cm^{-1}, making SnS_2 promising for single or tandem photoanodes or photovoltaics.[27] Additionally, its large bandgap may also take the advantages of suppressing drain to source tunneling for short channels in the aggressively integrated circuits nowadays.[13,28–30] MoS_2 nanoparticles or nanosheets are potential electrocatalysts for hydrogen evolution reaction (HER), and metallic 1T-MoS_2 can be much more active than semiconducting 2H-MoS_2, which have been indicated by experimental and theoretical studies.[13] The energies of the conduction and valence bands of SnS_2 single crystal range over the oxidation and reduction potentials of water, making it promising for water splitting.[27] Furthermore, the interlayer spacing of SnS_2 provides sites for intercalation of Cu or Co ions. Co intercalated SnS_2 exhibits a metal-like behavior with sheet resistance comparable to that of graphene.[41] The metallic Co-SnS_2 can be much more

Dr. L. P. Xu, Dr. X. Wang, Dr. F. F. Chen, Prof. Z. G. Hu, Dr. L. Y. Shang, Dr. J. Z. Zhang, Dr. K. Jiang, Prof. J. H. Chu
Technical Center for Multifunctional Magneto-Optical Spectroscopy (Shanghai)
Department of Materials
School of Physics and Electronic Science
East China Normal University
Shanghai 200241, P. R. China
E-mail: zghu@ee.ecnu.edu.cn
Dr. P. Zhang, Dr. H. N. Jiang, Prof. Y. J. Gong
School of Materials Science & Engineering
Beihang University
Beijing 100191, P. R. China
E-mail: yongjigong@buaa.edu.cn
Prof. Z. G. Hu, Prof. J. H. Chu
Collaborative Innovation Center of Extreme Optics
Shanxi University
Taiyuan 030006, Shanxi, P. R. China
Prof. Z. G. Hu, Prof. J. H. Chu
Shanghai Institute of Intelligent Electronics & Systems
Fudan University
Shanghai 200433, P. R. China
The ORCID identification number(s) for the author(s) of this article can be found under https://doi.org/10.1002/smll.201904116.

DOI: 10.1002/smll.201904116

active than its semiconducting counterpart as electrocatalysts for HER. Therefore, the controllable synthesis of high-quality, large-scale atomic-layer SnS_2 is the first step for its industrial applications in catalysis and electronics at the system level.[31,32]

So far, several methods including mechanical exfoliation (ME),[26,28,33–35] solution-based processes,[36–38] and chemical vapor deposition (CVD)[30–32,39–41] are adopted to prepare thin slabs of 2D SnS_2 for basic research purpose. However, 2D materials obtained by solution-assisted process or exfoliation of bulk material lack the controllability in uniformity, size, and thickness of the nanosheets, which may hinder its industrial applications in catalysis and electronics. CVD is known to be the most successful method for the synthesis of single-crystalline 2D semiconductors, due to the advantage over the precise control on morphology, defects, and structure of final products, particularly on large-scale atomic layer 2D material such as MoS_2, $MoSe_2$, and their heterostructures.[42,43] Although large-scale SnS_2 sheets have been synthesized via CVD, there are some problems, such as limitation in size and the difficulties in controlling the uniformity and the thickness of the final products, which dominate the layered semiconducting properties responsible for large-scale industrial catalysis and device applications. Thus, the growth of large-scale and high-quality SnS_2 with a controlled number of layers for practical applications is still needed.[31]

Herein, using a simple and scalable salt-assisted CVD method, we successfully synthesize large-size and high-quality SnS_2 atomic layers. The lateral size of SnS_2 can be as long as 410 μm and the layer numbers can be controlled from bilayer to bulk. The relationship between thickness and Raman active phonon mode was established, allowing the direct determination of the SnS_2 layer number through Raman spectroscopy. The high-quality lattice of SnS_2 with 2H stacking between different layers was observed by atomic resolution scanning transmission electron microscopy (STEM). Furthermore, the ultrathin SnS_2 nanosheet-based field-effect transistors (FETs) show a high on/off ratio about 10^8 and a carrier mobility of 2.58 $cm^2\ V^{-1}\ s^{-1}$, suggesting the potential applicability of SnS_2 in low-power consumption FETs. Additionally, such a good performance of 2D SnS_2 together with its controllable approach would allow us to unlock its electrocatalytic abilities for energy storage applications such as HER, oxygen evolution reaction (OER), and oxygen reduction reaction (ORR).

2. Results and Discussion

Large-size ultrathin SnS_2 nanosheets were synthesized via a salt-assisted CVD method, which is schematically illustrated in **Figure 1**a. Salt-assisted CVD method can be applied for the synthesis of a wide variety of the 2D TMDs. The salt is added as the reactant to decrease the melting and boiling point of the metal precursors and facilitate the formation of intermediate products, increasing the overall reaction rate. Briefly, a mixture of SnO_2 and KI was utilized as the metal precursor and was put at the center of the heating zone. KI can increase mass flux by reducing the melting point of SnO_2, thus increasing the rate of the reaction.[15] More details can be found in the Experimental Section. Low-magnification optical microscopy (OM) and scanning electron microscope (SEM) images are shown in Figure 1b and Figure S2a,b in the Supporting Information, respectively. We can see that the large amounts of SnS_2 nanosheets with average side length over 100 μm were uniformly distributed on the SiO_2/Si substrate. Figure 1c,d shows enlarged OM images of the as-grown SnS_2 nanosheets. Figure 1c,d reveals that the lateral size of SnS_2 nanosheets with high uniformity can be as long as 270 μm. The largest crystal is about 410 μm in edge [see Figure S1b in the Supporting Information; Figure 1e]. The large size of SnS_2 can promote device fabrication and corresponding characterizations. A SEM image of a triangular-shaped SnS_2 nanosheet depicted in Figure 1f indicates that the SnS_2 nanosheet has a clean and ultrathin surface. Atomic force microscopy (AFM) image of as-grown SnS_2 nanosheet is shown in Figure 1g. The section analysis [inset of Figure 1g] shows a thickness of about 1.5 nm, which confirms the bilayer feature.

From Figure 1, we can see that different shapes varying from triangle, windmill, to dendritic were achieved in this work. The shape of SnS_2 mainly depends on the distance between substrate and the mixture of SnO_2 and KI. For a short distance, the vapor pressure is relatively large, contributing to an irregular shape like the image in Figure 1d, in which SnS_2 first grows along three directions at an angle of 120° while the growth rate along other directions is distinctly slower. As shown in Figure 1c, the difference of growth rate becomes smaller when the distance becomes longer. For a larger distance, the vapor pressure is appropriate to ensure consistent growth rates along different directions and finally SnS_2 nanosheets with a common triangle shape can be obtained.

To develop further insight into the composition and chemical states of the as-grown SnS_2 nanosheet, X-ray photoelectron spectroscopy (XPS) was performed. A representative XPS spectrum of SnS_2 is shown in **Figure 2**a. The Sn 3d peak splits due to spin–orbit coupling to form separate peaks $3d_{3/2}$ and $3d_{5/2}$ at binding energy of 495.3 and 486.8 eV, respectively, indicating Sn^{4+} oxidation state. In the case of anions, for S we observe two characteristic peaks corresponding to $2p_{3/2}$ (163.7 eV) and $2p_{1/2}$ (164.8 eV), confirming it as S^{2-} state. Raman spectroscopy is a versatile tool for the study of the crystal structure, quality, and the number of layers of 2D material, such as graphene, MoS_2, and others.[32,44,45] Figure 2b,c shows an optical image of a triangular SnS_2 single crystal and its corresponding Raman intensity mapping at 315 cm^{-1}, respectively. The uniform Raman intensity in the map indicates highly homogeneous distribution of SnS_2 across the sheet. The regular color change of the optical image reflects the thickness and number of layers.[46] An optical image of SnS_2 nanosheet with different layers is shown in Figure 2d. From the edge to the center, the optical color contrast between different layers is clear. Clearly, the bright yellow regions indicate bulk Sn_2 crystal, while the atomic layers appear in blue color. Bilayer, three-layer, and four-layer regions are marked as 2, 3, and 4, respectively, which are selected on purpose to study the layer number dependence of Raman spectra. Figure 2e depicts the typical Raman spectra of a multilayer SnS_2 characterized by a 532 nm laser recorded at room temperature. The most intense peak at 315 cm^{-1} is assigned as A_{1g} mode, which belongs to the characteristic peak of SnS_2. The frequency of A_{1g} mode shows a blueshift as the

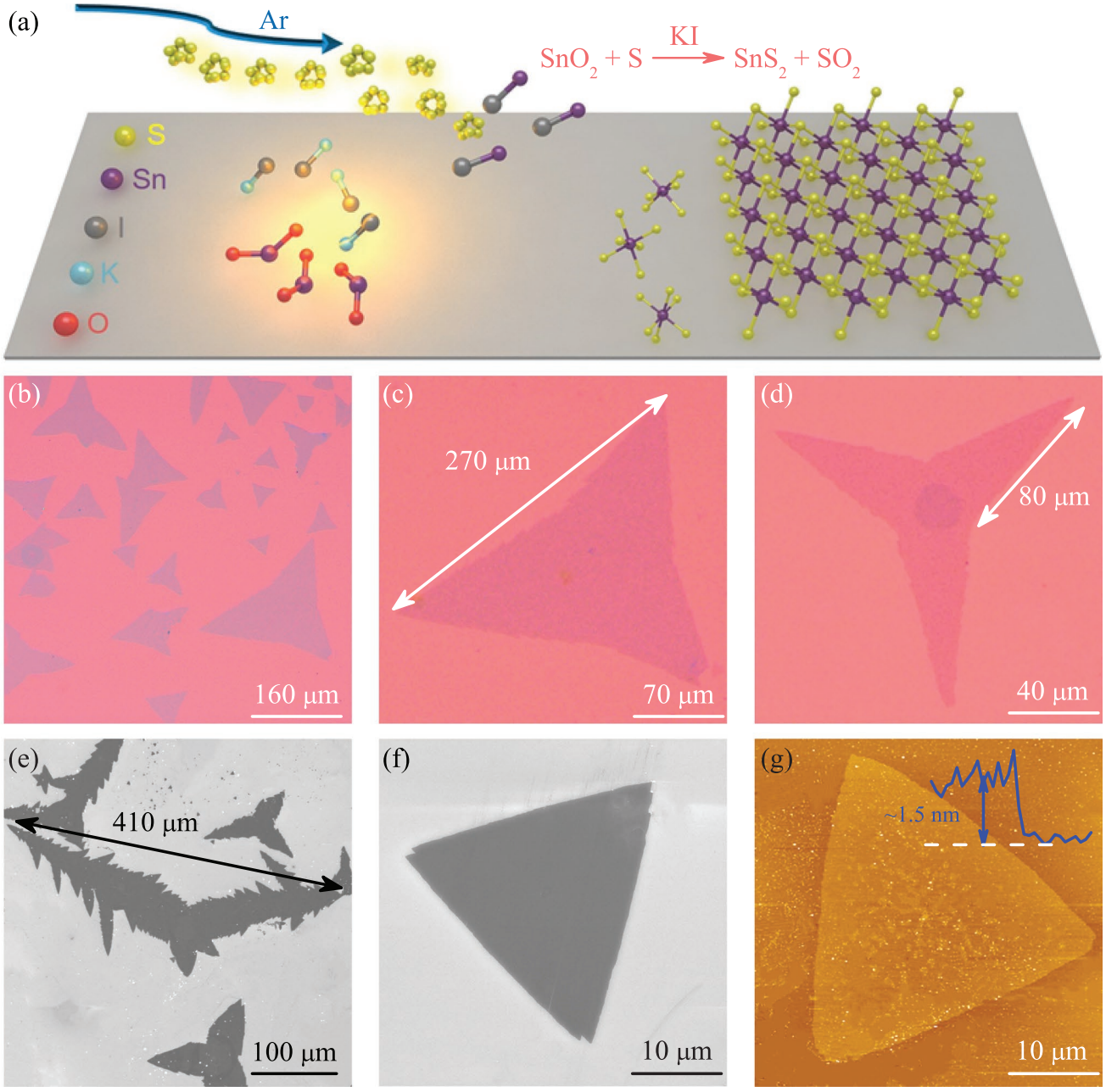

Figure 1. a) Schematic representation for the synthesis process of SnS_2 by CVD. b) A low-magnification optical image to show high yield of SnS_2 atomic layers. c,d) The typical optical microscopy images of SnS_2 single crystals. The lateral size of the SnS_2 single crystals can be as long as 270 μm. e,f) SEM images of as-grown SnS_2. The large-scale SnS_2 atomic layer is shown in (e), which is larger than 400 μm. g) AFM image of a resultant bilayer SnS_2. The inset is height profile along the white dashed line in (g).

thickness increases. Figure 2f shows the layer number dependence of A_{1g} peak, in which the intensity and the peak position both have an obvious increase. Specifically, from the bilayer to four-layer samples, the peak shifts from 311.5, 312.2, to 313.4 cm^{-1}. These changes give a quick and accurate way to determine the thickness of the SnS_2 atomic layers.

The investigations of the vibrational properties of TMDs are important to study the electron–phonon interaction, which plays a remarkable role in the electronic behavior of nanodevices and can affect the charge carrier mobility.[47–50] A systematic study of the vibrational properties of CVD grown in a wide temperature range is still lacking in the literature. Figure 2g represents typical Raman shift of bilayer and few-layer SnS_2 versus temperature plots. It is clearly seen that there is a redshift trend in the peak positions with increasing the temperature. Further, an increase in the full width at half maximum (FWHM) of the peak was observed for different layers of SnS_2 with increasing temperature recorded in this work. Figure S3a–d shows the temperature dependent Raman spectroscopy studies of SnS_2 from bilayer to a few layers. Apparently, the temperature

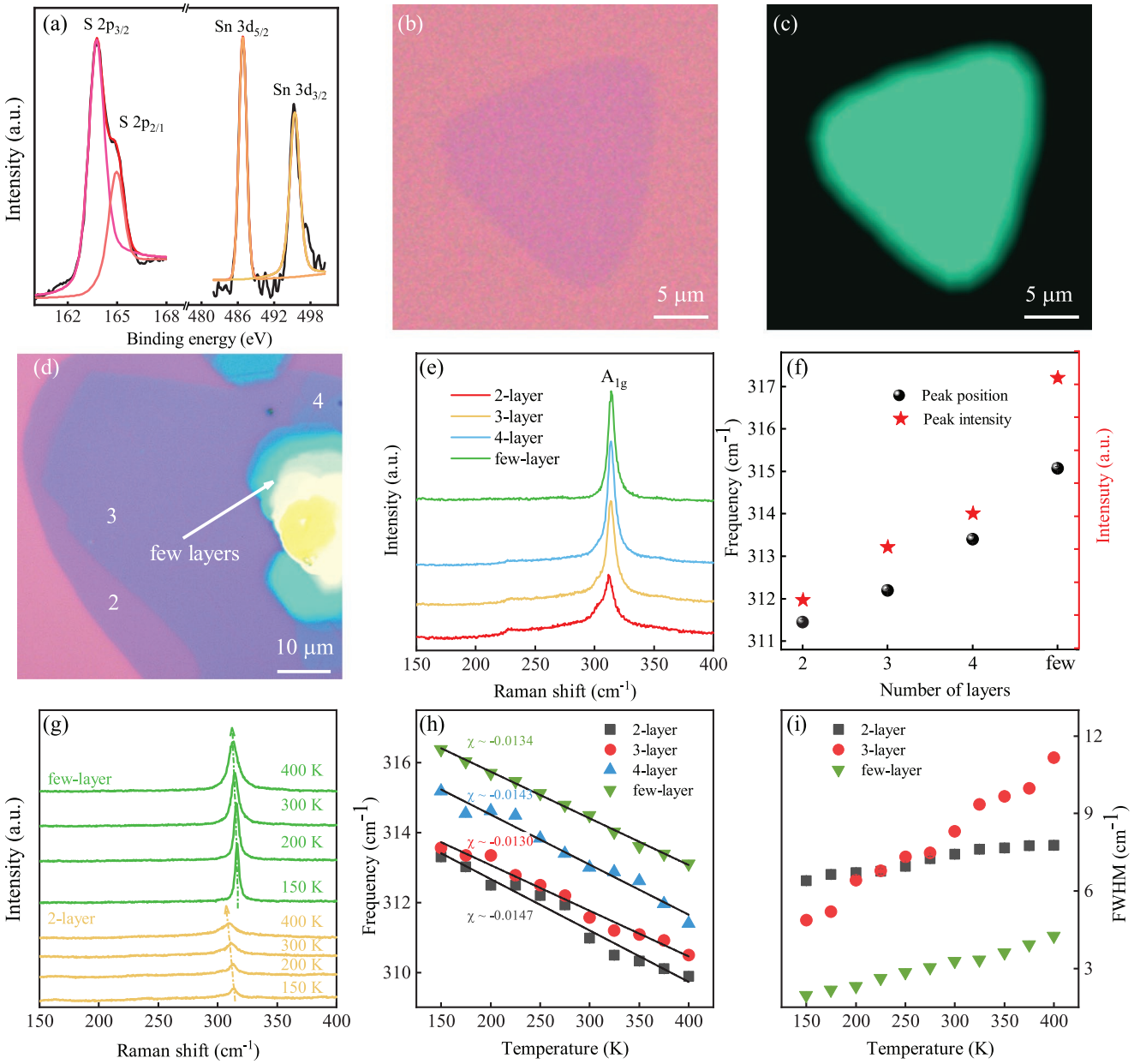

Figure 2. a) XPS spectrum showing binding states of S 2p and Sn 3d. b) Optical image of a triangular SnS_2 single crystal and c) the corresponding Raman mapping of the A_{1g} mode. d) Optical microscopy image of ultrathin SnS_2 with different layers, the layer numbers are marked out. e) Raman spectra of SnS_2 layers from bilayer to few-layer, the laser wavelength is 532 nm. f) Frequency (left vertical axis) and peak intensity (right vertical axis) of A_{1g} Raman mode for SnS_2 as a function of layer thickness. g) Raman spectra of bilayer and few-layer SnS_2 at different temperatures. h) Raman spectra peak position of A_{1g} mode as a function of temperature for different layered SnS_2. i) FWHM of A_{1g} mode as a function of temperature for different layered SnS_2.

dependence of the Raman spectra of SnS_2 with different thickness is similar to each other. Figure 2h shows the typical plots for Raman spectra peak positions as a function of temperature for SnS_2 with different thickness. The Raman modes decrease linearly with the temperature range from 150 to 400 K. The Raman peak positions for A_{1g} mode of different layered SnS_2 as a function of temperature were calculated by fitting the Lorentzian functions given by the following equation[48]

$$\omega(T) = \omega_0 + \chi T \quad (1)$$

where ω_0 and χ are the peak position of A_{1g} mode at zero Kelvin temperature and the first order temperature coefficient of A_{1g} mode, respectively. The temperature coefficient χ comes from the slope of the fitted straight line. The calculated values of temperature coefficients χ are −0.0147, −0.0130, −0.0143, and −0.0134, corresponding to bilayer, 3-layer, 4-layer, and few-layer, respectively. The change in the peak positions with the temperature is mostly due to the contribution from the thermal anharmonicity, i.e., from thermal expansion and volume contribution. The FWHM of A_{1g} mode as a function of temperature

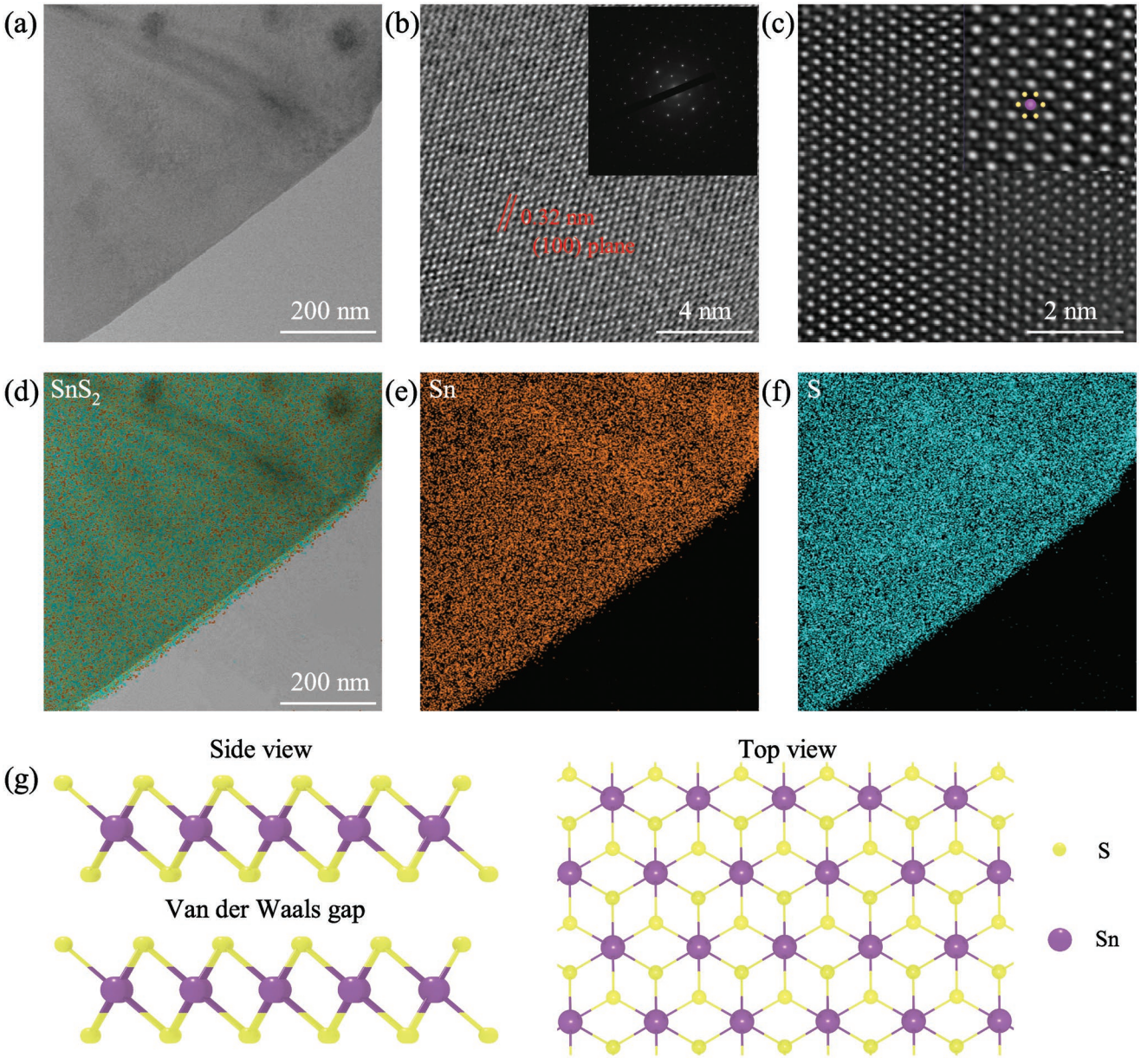

Figure 3. a) Conventional TEM image of the sample. b) ADF-STEM image of SnS_2, inset shows the corresponding FFT pattern, revealing the hexagonal structure and high crystal quality. c) ADF-STEM image of SnS_2 shows its perfect hexagonal lattice. Inset shows the enlarged TEM image. d–f) Corresponding EDS mapping of SnS_2, Sn, and S, respectively. g) Schematic diagram of the side view and top view of hexagonal structure of SnS_2.

for different layered SnS_2 is shown in Figure 2i. The broadening in FWHM with temperature is mainly due to the contribution from the decay of a zone center optical phonon into one acoustic and one optical phonon.[48]

Then, we used high-resolution transmission electron microscope (HRTEM) equipped with an energy-dispersion X-ray detector to further confirm the atomic structure and quality of the KI assisted growth of SnS_2. **Figure 3**a shows the morphology of the bright field images of as-transferred SnS_2, confirming a smooth and clear surface. Figure 3b depicts the high-resolution transmission electron microscope of the corresponding area in Figure 3a. A clear hexagonal structure without atomic vacancies or distortions can be observed from the TEM image. The lattice distance is measured to be 0.32 nm, which can be assigned as (100) plane of SnS_2 and agrees well with the known value of 0.317 nm for SnS_2 crystal. The selected-area electron diffraction (SAED) image in the inset of Figure 3b further confirms the hexagonal lattice of SnS_2 and the strikingly high crystal quality of as-grown SnS_2. The atomic resolution high-angle annular dark field (HAADF) image of SnS_2 is shown in Figure 3c, where the intensity contrast of bright and dark atoms corresponds to the Sn and S atoms, respectively. Inset of Figure 3c shows the enlarged TEM image. From the top view, it is clear that one Sn atom is surrounded by six

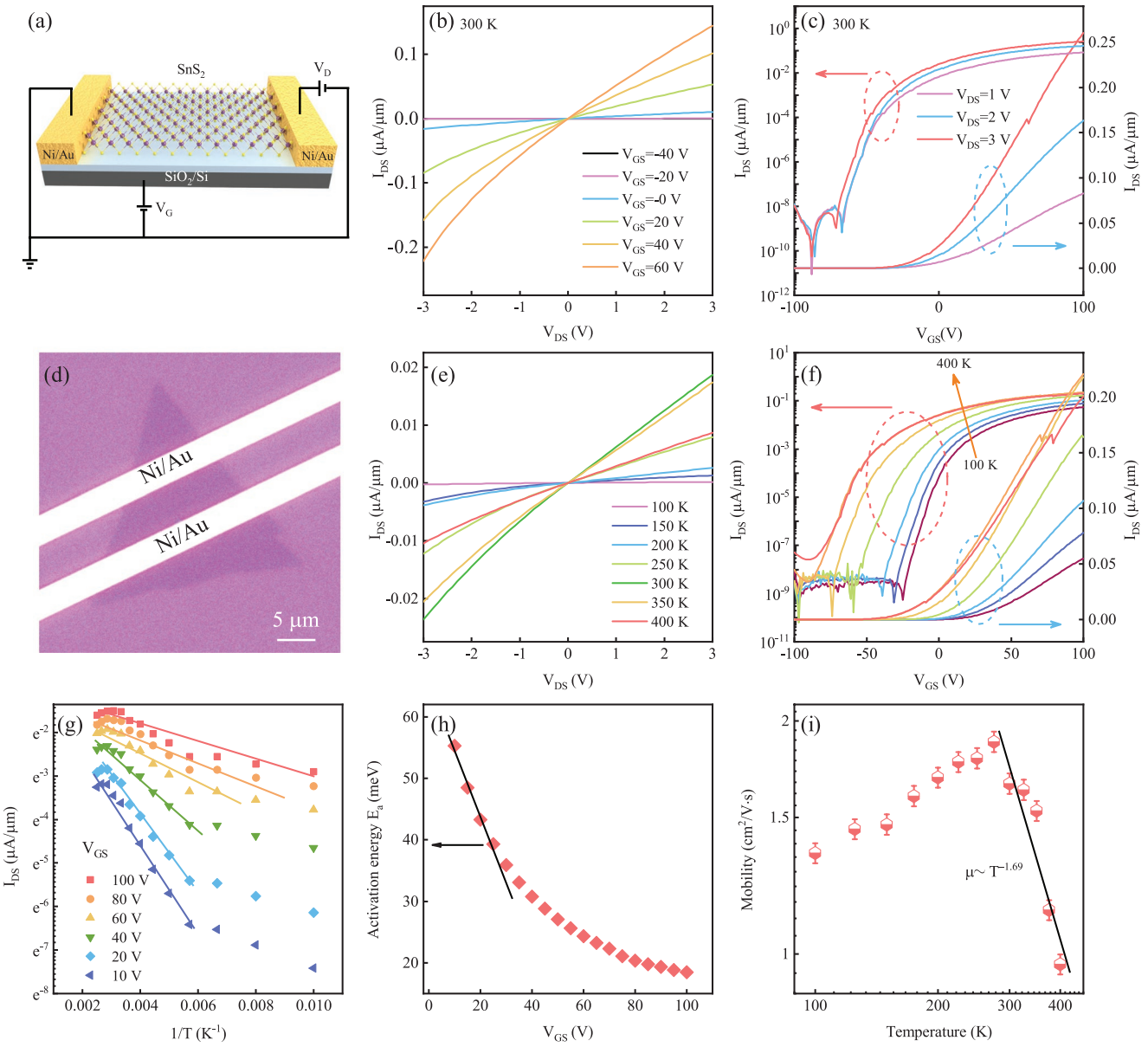

Figure 4. a) Schematic diagram of the SnS_2-based FET. b,c) Electrical output and transfer curve of SnS_2 device. Back-gate voltage (V_{GS}) sweeping: −40 to 60 V; source–drain bias (V_{DS}): 1 to 3 V. d) A typical optical image of a SnS_2 device on 300 nm SiO_2/Si. e,f) Measurement-temperature-dependent electrical output and transfer curve of SnS_2 device. g) The temperature dependence of I_{DS} is plotted using the thermally activated transport model for different values of V_{GS}. h) Dependence of activation energy E_a on V_{GS}. i) Field effect mobility as a function of temperature.

nearest-neighbor S atoms, which is the feature of the 1T phase. Figure 3g represents the side and top view atomic structure of 1T phase of SnS_2. As 1T structure of monolayer SnS_2, the 2H stacking of each monolayer SnS_2 is similar to the bulk crystal, where the sulfur and tin in one layer aligned with sulfur and tin in another layer, forming a sandwich-like structure. Furthermore, energy dispersive X-ray spectroscopy (EDS) mapping was employed to explore the chemical compositions of SnS_2 nanosheet shown in Figure 3d–f, indicating the unform distribution of Sn and S elements. The EDS spectrum of the SnS_2 nanosheet depicted in Figure S4b in the Supporting Information shows clear signals of S and Sn with an atomic ratio of 1.95:1, which confirms that SnS_2 samples grown by CVD are n-type semiconductors because of sulfur deficiency.[41]

To further illustrate the potential application of SnS_2, back-gated FETs were fabricated on heavily doped silicon substrates with a 300 nm SiO_2 layer. **Figure 4**a,d shows the schematic and optical image of a typical SnS_2 FET device, respectively. The patterned Ni/Au (2/50 nm) electrodes were deposited by thermal evaporation, with a channel length of 5 μm and width of 20 μm. Concrete details can be found in the Experimental Section. The output and transfer characteristics of the device recorded at room temperature in the dark condition are shown in Figure 4b,c. The drain–source current as shown in

Figure 4b linearly increased as the bias rising from −3 to +3 V, indicating an ohmic contact between Ni/Au electrodes and SnS_2 channel. As the gate voltage is swept from V_{GS} = −100 to +100 V, the FET SnS_2 conduction channel switches from an insulating state to a conducting state. This n-type FET behavior in the SnS_2 device agrees with EDS result (sulfur deficiency), indicating electron doping in as-grown SnS_2 materials. When a positive gate voltage is applied, electrons (the majority carrier) are accumulated in the conduction channel so that the current I_{DS} first increases and then tends to saturate at higher voltage. At negative V_{GS}, electrons are depleted, resulting in a suppressed electrical conductance. The corresponding on/off current ratio, extracted from the logarithmic plot of I_{DS} versus V_{GS} (Figure 4c), is found to exceed 10^7, which is an order of magnitude higher than the previously reported value (10^6) of mechanical exfoliated SnS_2.[28,33] The field effect mobility (μ_e) of the ultrathin SnS_2 channel can be calculated by the following equation

$$\mu_e = \frac{dI_{DS}}{dV_{DS}} \cdot \frac{L}{WC_iV_{DS}} \quad (2)$$

where L and W are the length and width of the device, and C_i is the capacitance per unit area (11.6 nF cm^{-2} for 300 nm SiO_2 layer in these experiments).[28] The calculated μ_e is about 2.58 cm^2 V^{-1} s^{-1} at room temperature, which is comparable with those SnS_2 FETs recently reported.[29,30]

To better understand the device physics, the cool-down measurements for the same device were also carried out. Figure 4e,f shows the typical output and transfer curves at various temperatures. With decreasing the temperature, the subthreshold slope of the FET becomes steeper, indicating a suppression of the substrate doping effect. The OFF current decreases significantly during the cooling. From these transfer curves, we find that the temperature variation of a typical conductance, G in the temperature regime between 100 and 325 K, can be modeled with thermally activated transport[51]

$$G = G_0(T)e^{-E_a/k_BT} \quad (3)$$

where E_a is the activation energy, k_B is the Boltzmann constant, and $G_0(T)$ is the temperature related parameter. Figure 4g shows the curve of $\ln I_{DS}$ versus $1/T$ for different V_{DS} values. The good agreement of the data with the activation model suggests that charge transport is thermally activated. From a linear fitting, the E_a value of 18 meV for V_{GS} = 100 V can be extracted, which is much smaller than the bandgap of SnS_2. This may result from the depth of the donor band located above the valence band caused by impurities or defects.[52] From the temperature dependence of conductance for different V_{GS}, the activation energy E_a dependence on V_{GS} can be extracted, which is shown in Figure 4h. When barrier tunneling becomes the dominant mechanism for charge carrier injection, the E_a deviates from the linear trend, from which we estimate a Schottky barrier height for the charge carrier injection from gold electrodes into SnS_2 of $\phi_{SB} \approx 38$ meV. This value is relatively small and does not have a significant influence on the mobility extraction. The temperature-dependent mobility of the FET is summarized in Figure 4i. Below 275 K, we observe a decrease of the mobility as the temperature down to 100 K. In this case, mobility is limited by scattering from charged impurities.[51] The mobility decreases with increasing the temperature, from the peak value of 1.88 cm^2 V^{-1} s^{-1} at a measurement-temperature of 275 K. This behavior is related to electron–phonon scattering that becomes the dominant mechanism at higher temperature. We fit the high measurement-temperature regime ($T \geq 275$ K) with the generic temperature dependence of the mobility $\mu \sim T^{-\alpha}$, where the exponent depends on the dominant phonon scattering mechanism. In this power-law dependence $T^{-\alpha}$, $\alpha = 1$ results from pure acoustic phonon scattering. When optical phonon scattering starts to dominate at higher temperature, the temperature dependence of mobility becomes stronger with $\alpha > 1$. In this regime, exponent relies on the optical phonon frequencies and electron–phonon coupling strength. From the fitting, we find the value of $\alpha = 1.69$. The theoretical prediction value of α for monolayer MoS_2 is 1.69.[53] Figure S5a,b in the Supporting Information represents the temperature dependence of I_{DS} (at V_{DS} = 3 V, V_{GS} = 0 V) and on/off ratio, respectively. With increasing the temperature, I_{DS} increases, reaching a maximum value of 0.024 μA μm^{-1} at 325 K, and then decreases at higher temperatures. The on/off ratio decreases linearly with the temperature.

We also employ the FETs based on CVD-grown SnS_2 nanosheets as photodetectors. **Figure 5**a presents I_{DS} versus V_{DS} curves at V_{GS} = 0 V under illumination with various laser power. As the illumination intensity increases from 0 to 313 mW cm^{-2}, the conductance raises by a factor of 22. Under illumination with a laser (the wavelength of 407 nm), electrons are injected into the conduction band and holes are left in the valence band. Both the photoinduced electrons and holes take part in the photoconductivity process. As can be seen in Figure 5b, we plot the dependent curve of photocurrent (I_{ph}) versus light power intensity (P). We also fit the curve with a power law, $I_{ph} \sim P^{\gamma}$, where the exponent γ generally locates in the range between 0 and 1 and reflects a complex process including the generation, separation, and recombination of photoinduced electron–hole pairs.[54] From the fitting, we observe the value of γ= 0.87, indicating the high quality of SnS_2 with few defects or traps. Due to energy levels inside the SnS_2 bandgap serving as charge trap states, electrons or holes would be trapped by trapping center. For example, if holes are trapped near the valence band, the electrons will stay in the conduction band for a longer time before combining with the holes. This effect leads to effective n-type doping and high external quantum efficiency but longer response time. In Figure S6 in the Supporting Information, the dark-state IV curve is slightly nonlinear with respect to the bias polarity, indicating the existence of a Schottky barrier between the electrodes and SnS_2. As the illumination intensity increases, the I–V curves become more and more linear and symmetric, due to photoinduced hot-carrier transport over the contact barriers. The pulse-response of a typical SnS_2 device is shown in Figure S6 in the Supporting Information. The long rise and fall times suggest that long-lived charge traps, which may result from the interface conditions between SnS_2 and SiO_2, are responsible for the observed slow response. These two factors, i.e., high external quantum efficiency and longer response time indicate the existence of trap states.

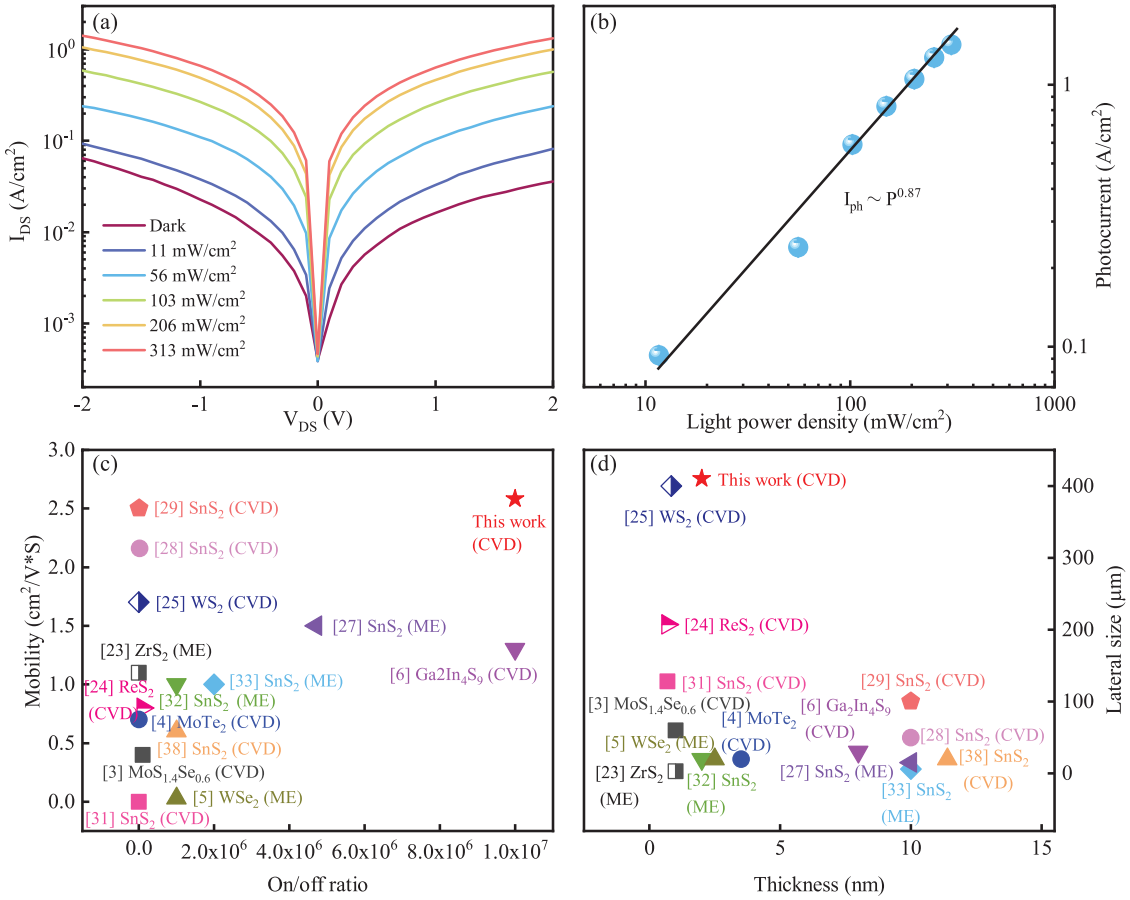

Figure 5. a) The drain current (I_{DS}) of SnS_2 phototransistor at V_{GS} = 0 V with different illumination powers from a laser with an excitation wavelength of 407 nm. b) The power-dependence of the photocurrent of SnS_2 phototransistor at V_{DS} = 3 V. c) The mobility and on/off ratio, and d) lateral size and thickness of our SnS_2-based FET as compared to recently reported FETs based on SnS_2 and other TMDs.

The performance of ultrathin SnS_2 nanosheet in the present work in comparison with many previously reported SnS_2 and other TMDs material-based devices are summarized in Figure 5. It is clear that the electrical properties of our SnS_2 FETs can rival or even surpass reported SnS_2 and other TMDs. The best mobility of our SnS_2 is 2.58 cm^2 V^{-1} s^{-1}, which is comparable to that of mechanical exfoliated SnS_2, which may result from the excellent crystallinity of the SnS_2 and the good contact between the electrodes and SnS_2 channel. Additionally, the S-atom deficiency, traps induced during the growth process may also contribute to the good performance of SnS_2. The on/off ratio from our SnS_2 FETs exceeds 10^7 and can be as high as 10^8. Furthermore, the lateral size of SnS_2 in the work can be as long as 410 μm, which can facilitate the scale-up device construction. Such excellent performance can be explained by high-quality character, large specific surface area, and surface trap states. The high surface areas are crucially important for energy storage, catalysis, and field-emitting applications. Moreover, the large-scale and high-quality SnS_2 sheets combined with intercalation engineering provide possibilities for the research of microcosmic mechanism regulated by electric field in HER.

Although, the performance of SnS_2 in this work is superior to other reported SnS_2-based FETs. In order to further improve the performance of SnS_2, we can reduce the amount of KI without deteriorating the growth of SnS_2. In addition, after taking out the samples from the furnace, the residual KI can be removed by soaking them in methanol or acetone immediately. What's more, KI can be replaced by SnC_2O_4 to avoid the effect of K and I ion during the growth process. The melting point and the vapor pressure of pure SnO_2 can be decreased and increased by a small amount of SnC_2O_4, respectively. The crystal quality may be improved if the ions of K and I were not introduced, which would be verified latter in the future experiments.

3. Conclusion

In conclusion, we synthesized large-size and high-quality ultrathin SnS_2 nanosheets with the lateral size of up to 410 μm via a KI assisted CVD method. Employing the salt can decrease the melting point of the reactants and facilitate the formation of intermediate products, which may contribute to forming a stable condition for growth of large-size nanosheets, might paving the way for electronics and optoelectronics applications. The as-grown SnS_2 nanosheets can be thinned to 1.5 nm (bilayer) in the present conditions. Specially, our ultrathin SnS_2 nanosheet-based FETs exhibit excellent performance,

including high mobility (2.58 cm^2 V^{-1} s^{-1}) and high on/off ratio (exceeding 10^7), superior to other reported SnS_2-based FETs. Furthermore, we systematically investigated the effects of temperature on electrical properties. Below 275 K, mobility is limited by scattering from charged impurities. While electron–phonon scattering becomes the dominant mechanism at higher temperature. Such a good performance of wide bandgap of 2D SnS_2 together with its controllable approach may open up opportunities for the emerging 2D materials in future applications of electrocatalysis, electronics, and optoelectronics.

4. Experimental Section

Growth of SnS_2 Layers: Large-scale SnS_2 nanosheets were grown via CVD method by using sulfur (S) and tin oxide (SnO_2) as precursors. Specifically, a powder mixture of 1 mg KI and 10 mg SnO_2 in an alumina boat was placed at the center of the furnace and SiO_2/Si substrates were placed on the top with the polished surface down. The temperature of the furnace was first heated to 650 °C with a ramp rate of 50 °C min^{-1} and this temperature was retained for another 5 min for the growth. 200 mg S was placed in an alumina boat at the upstream and the temperature of S was about 200 °C during the growth. Argon with a flow rate of 50 sccm was used as carrier gas and to keep an inert atmosphere. The whole process was under atmospheric pressure.

Fabrication of Devices: The source and drain electrodes were patterned on few-layer SnS_2 using electron beam lithography (EBL). The Ni/Au (2/50 nm) electrodes were deposited using the thermal evaporator, followed by the lift off process. The heavily Si substrate and the SiO_2 of 300 nm served as the back-gated electrode and dielectric, respectively. Electrical measurements were performed using a Janis ST-500 cryogenic probe station at the base pressure of 10^{-6} Torr. The device electrodes were connected to a Keithley 4200-SCS semiconductor parameter analyzer. The laser with the wavelength of 407 nm was used to measure the photoresponse of the devices.

Characterizations: SEM was performed using a Zeiss scanning electron microscope at the accelerating voltage of 10 kV. The morphology and thickness of SnS_2 flakes were characterized using commercial atomic force microscope system (Dimension Icon, Bruker) with ScanAsyst modes. Raman spectra were recorded using a confocal micro-Raman spectrometer (Jobin-Yvon LabRAM HR Evolution, Horiba) with the excitation laser of 532 nm and a THMSE 600 heating/cooling stage (Linkam Scientific Instruments) in the temperature range from 150 to 400 K with a resolution of 0.1 K. Chemical configurations were determined by XPS (Phi V5000). XPS measurements were performed with an Mg Kα X-ray source on the sample. The energy calibrations were made against the C 1s peak to eliminate the charging of the sample during analysis. EDS elemental analysis was performed by JEOL ARM-200CF. The SnS_2 nanosheets were transferred onto a copper grid for TEM observation. STEM imaging was performed on JEOL ARM-200CF operated at 80 kV.

Supporting Information

Supporting Information is available from the Wiley Online Library or from the author.

Acknowledgements

L.P.X., P.Z., and H.N.J. contributed equally to this work. This work was financially supported by the National Key R&D Program of China (grant nos. 2017YFA0303403, 2018YFB0406500, and 2018YFA0306900), the National Natural Science Foundation of China (grant nos. 61674057, 91833303, and 51872012), the Projects of Science and Technology Commission of Shanghai Municipality (grant nos. 18JC1412400, 18YF1407200, and 18YF1407000), and the Program for Professor of Special Appointment (Eastern Scholar) at Shanghai Institutions of Higher Learning.

Conflict of Interest

The authors declare no conflict of interest.

Keywords

chemical vapor deposition, field-effect transistors, large scale, SnS_2, van der Waals layered materials

Received: July 27, 2019
Revised: August 28, 2019
Published online: October 7, 2019

[1] S. Manzeli, D. Ovchinnikov, D. Pasquier, O. V. Yazyev, A. Kis, *Nat. Rev. Mater.* **2017**, *2*, 17033.
[2] M. Okada, T. Sawazaki, K. Watanabe, T. Taniguch, H. Hibino, H. Shinohara, R. Kitaura, *ACS Nano* **2014**, *8*, 8273.
[3] Q. L. Feng, Y. M. Zhu, J. H. Hong, M. Zhang, W. J. Duan, N. N. Mao, J. X. Wu, H. Xu, F. L. Dong, F. Lin, C. H. Jin, C. M. Wang, J. Zhang, L. M. Xie, *Adv. Mater.* **2014**, *26*, 2648.
[4] R. Ma, H. R. Zhang, Y. D. Yoo, Z. P. Degregorio, L. Jin, P. Golani, J. G. Azadani, T. Low, J. E. Johns, L. A. Bendersky, A. V. Davydov, S. J. Koester, *ACS Nano* **2019**, *13*, 8035.
[5] A. N. Hoffman, M. G. Stanford, C. Zhang, I. N. Ivanov, A. D. Oyedele, M. G. Sales, S. J. McDonnell, M. R. Koehler, D. G. Mandrus, L. B. Liang, B. G. Sumpter, K. Xiao, P. D. Rack, *ACS Appl. Mater. Interfaces* **2018**, *10*, 36540.
[6] F. K. Wang, T. Gao, Q. Zhang, Z. Y. Hu, B. Jin, L. Li, X. Zhou, H. Q. Li, G. V. Tendeloo, T. Y. Zhai, *Adv. Mater.* **2019**, *31*, 1806306.
[7] Y. H. Chang, W. J. Zhang, Y. H. Zhu, Y. Han, J. Pu, J.-K. Chang, W.-T. Hsu, J.-K. Huang, C.-L. Hsu, M.-H. Chiu, T. Takenobu, H. N. Li, C. Wu, W. H. Chang, A. T. S. Wee, L. J. Li, *ACS Nano* **2014**, *8*, 8582.
[8] C. L. Tan, H. Zhang, *Chem. Soc. Rev.* **2015**, *44*, 2713.
[9] H. Zhang, *ACS Nano* **2015**, *9*, 9451.
[10] Q. P. Lu, Y. F. Yu, Q. L. Ma, B. Chen, H. Zhang, *Adv. Mater.* **2016**, *28*, 1917.
[11] X. Huang, Z. Y. Zeng, S. Y. Bao, M. F. Wang, X. Y. Qi, Z. X. Fan, H. Zhang, *Nat. Commun.* **2013**, *4*, 1444.
[12] Z. Y. Yin, B. Chen, M. Bosman, X. H. Cao, J. Z. Chen, B. Zheng, H. Zhang, *Small* **2014**, *10*, 3537.
[13] X. L. Chen, X. B. Lu, B. C. Deng, O. Sinai, Y. C. Shao, C. Li, S. F. Yuan, V. Tran, K. Watanabe, T. Taniguchi, D. Naveh, L. Yang, F. N. Xia, *Nat. Commun.* **2017**, *8*, 1672.
[14] J. P. Shi, X. N. Wang, S. A. Zhang, L. F. Xiao, Y. H. Huan, Y. Gong, Z. P. Zhang, Y. C. Li, X. B. Zhou, M. Hong, Q. Y. Fang, Q. Zhang, X. F. Liu, L. Gu, Z. F. Liu, Y. F. Zhang, *Nat. Commun.* **2017**, *8*, 958.
[15] J. D. Zhou, J. H. Lin, X. W. Huang, Y. Zhou, Y. Chen, J. Xia, H. Wang, Y. Xie, H. M. Yu, J. C. Lei, D. Wu, F. C. Liu, Q. D. Fu, Q. S. Zeng, C. H. Hsu, C. L. Yang, L. Liu, T. Yu, Z. X. Shen, H. Lin, B. I. Yakobson, Q. Liu, K. Suenaga, G. T. Liu, Z. Liu, *Nature* **2018**, *556*, 355.
[16] X. P. Cui, Z. Z. Kong, E. L. Gao, D. Z. Huang, Y. Yao, H. G. Shen, C. A. Di, Z. P. Xu, J. Zheng, D. B. Zhu, *Nat. Commun.* **2018**, *9*, 1301.

[17] A. Li, Q. X. Chen, P. P. Wang, Y. Gan, T. L. Qi, P. Wang, F. D. Tang, J. Z. Wu, R. Chen, L. Y. Zhang, Y. P. Gong, *Adv. Mater.* **2019**, *31*, 1805656.
[18] S. Q. Guo, D. Yang, S. Zhang, Q. Dong, B. C. Li, N. Tran, Z. Y. Li, Y. J. Xiong, M. E. Zaghloul, *Adv. Funct. Mater.* **2019**, *29*, 1900138.
[19] A. Splendiani, L. Sun, Y. B. Zhang, T. S. Li, J. Kim, C. Y. Chim, G. Galli, F. Wang, *Nano Lett.* **2010**, *10*, 1271.
[20] K. F. Mak, C. G. Lee, J. Hone, J. Shan, T. F. Heinz, *Phys. Rev. Lett.* **2010**, *105*, 136805.
[21] M. Langer, M. Kisiel, R. Pawlak, F. Pellegrini, G. E. Santoro, R. Buzio, A. Gerbi, G. Balakrishnan, A. Baratoff, E. Tosatti, E. Meyer, *Nat. Mater.* **2014**, *13*, 173.
[22] K. Chen, Z. F. Chen, X. Wan, Z. B. Zheng, F. Y. Xie, W. J. Chen, X. C. Gui, H. J. Chen, W. G. Xie, J. B. Xu, *Adv. Mater.* **2017**, *29*, 1700704.
[23] M. Zhang, Y. M. Zhu, X. S. Wang, Q. L. Feng, S. L. Qiao, W. Wen, Y. F. Chen, M. H. Cui, J. Zhang, C. Z. Cai, L. M. Xie, *J. Am. Chem. Soc.* **2015**, *137*, 7051.
[24] F. F. Cui, Q. L. Feng, J. H. Hong, R. Y. Wang, Y. Bai, X. B. Li, D. Y. Liu, Y. Zhou, X. Liang, X. X. He, Z. Y. Zhang, S. Z. Liu, Z. B. Lei, Z. H. Liu, T. Y. Zhai, H. Xu, *Adv. Mater.* **2017**, *29*, 1705015.
[25] B. S. Tang, Z. G. Yu, L. Huang, J. W. Chai, S. L. Wong, J. Deng, W. F. Yang, H. Gong, S. J. Wang, K. W. Ang, Y. W. Zhang, *ACS Nano* **2018**, *12*, 2506.
[26] S. A. Hosseini, A. Esfandiar, A. I. Zad, S. H. Hosseini-Shokouh, S. M. Mahdavi, *ACS Photonics* **2019**, *6*, 728.
[27] B. Giri, M. Masroor, T. Yan, K. Kushnir, A. D. Carl, C. Doiron, H. C. Zhang, Y. Y. Zhao, A. McClelland, G. A. Tompsett, D. W. Wang, R. L. Grimm, L. V. Titova, P. M. Rao, *Adv. Energy Mater.* **2019**, *2*, 1901236.
[28] Y. Huang, E. Sutter, J. T. Sadowski, M. Cotlet, O. L. Monti, D. A. Racke, M. R. Neupane, D. Wickramaratne, R. K. Lake, B. A. Parkinson, P. Sutter, *ACS Nano* **2014**, *8*, 10743.
[29] J. H. Ahn, M. J. Lee, H. Heo, J. H. Sung, K. Kim, H. Hwang, M. H. Jo, *Nano Lett.* **2015**, *15*, 3703.
[30] X. Zhou, Q. Zhang, L. Gan, H. Q. Li, T. Y. Zhai, *Adv. Funct. Mater.* **2016**, *26*, 4405.
[31] G. Su, V. G. Hadjiev, P. E. Loya, J. Zhang, S. Lei, S. Maharjan, P. Dong, P. M. Ajayan, J. Lou, H. Peng, *Nano Lett.* **2015**, *15*, 506.
[32] G. Ye, Y. Gong, S. Lei, Y. He, B. Li, X. Zhang, Z. H. Jin, J. Lou, R. Vajtai, W. Zhou, P. M. Ajayan, *Nano Res.* **2017**, *10*, 2386.
[33] H. S. Song, S. L. Li, L. Gao, Y. Xu, K. Ueno, J. Tang, Y. B. Cheng, K. Tsukagoshi, *Nanoscale* **2013**, *5*, 9666.
[34] D. De, J. Manongdo, S. See, V. Zhang, A. Guloy, H. B. Peng, *Nanotechnology* **2013**, *24*, 025202.
[35] H. T. Yuan, M. Toh, K. Morimoto, W. Tan, F. Wei, H. Shimotani, C. Kloc, Y. Iwasa, *Appl. Phys. Lett.* **2011**, *98*, 012102.
[36] X. S. Wang, Z. W. Wang, J. D. Zhang, X. Wang, Z. P. Zhang, J. J. Wang, Z. H. Zhu, Z. Y. Li, Y. Liu, X. F. Hu, J. W. Qiu, G. H. Hu, B. Chen, N. Wang, Q. Y. He, J. Z. Chen, J. X. Yan, W. Zheng, T. Hasan, S. Z. Li, H. Li, H. Zhang, Q. Wang, X. Huang, W. Huang, *Nat. Commun.* **2018**, *9*, 3611.
[37] Y. Tao, X. Wu, W. Wang, J. Wang, *J. Mater. Chem. C* **2015**, *3*, 1347.
[38] Y. D. Zhang, P. Y. Zhu, L. L. Huang, J. Xie, S. C. Zhang, G. S. Cao, X. B. Zhao, *Adv. Funct. Mater.* **2015**, *25*, 481.
[39] B. Li, L. Huang, M. Z. Zhong, Y. Li, Y. Wang, J. B. Li, Z. M. Wei, *Adv. Electron. Mater.* **2016**, *2*, 1600298.
[40] J. Xia, D. D. Zhu, L. Wang, B. Huang, X. Huang, X. M. Meng, *Adv. Funct. Mater.* **2015**, *25*, 4255.
[41] Y. J. Gong, H. T. Yuan, C. L. Wu, P. Z. Tang, S. Z. Yang, A. K. Yang, G. D. Li, B. F. Liu, J. Groep, M. L. Brongerama, M. F. Chisholm, S. C. Zhang, W. Zhou, Y. Cui, *Nat. Nanotechnol.* **2018**, *13*, 294.
[42] Y. J. Gong, J. H. Lin, X. L. Wang, G. Shi, S. D. Lei, Z. Lin, X. L. Zou, G. L. Ye, R. Vajtai, B. I. Yakobson, H. Terrones, M. Terrones, B. K. Tay, J. Lou, S. T. Pantelides, Z. Liu, W. Zhou, P. M. Ajayan, *Nat. Mater.* **2014**, *13*, 1135.
[43] Y. J. Gong, S. D. Lei, G. L. Ye, B. Li, Y. M. He, K. Keyshar, X. Zhang, Q. Z. Wang, J. Lou, Z. Liu, R. Vajtai, W. Zhou, P. M. Ajayan, *Nano Lett.* **2015**, *15*, 6135.
[44] C. G. Lee, H. G. Yan, L. E. Brus, T. F. Heinz, J. Hone, S. M. Ryu, *ACS Nano* **2010**, *4*, 2695.
[45] H. Li, G. Lu, Z. Y. Yin, Q. Y. He, H. Li, Q. Zhang, H. Zhang, *Small* **2012**, *8*, 682.
[46] Y. D. Zhao, J. S. Qiao, P. Yu, Z. X. Hu, Z. Y. Lin, S. P. Lau, Z. Liu, W. Ji, Y. Chai, *Adv. Mater.* **2016**, *28*, 2399.
[47] Q. H. Wang, K. Kalantar-Zadeh, A. Kis, J. N. Coleman, M. S. Strano, *Nat. Nanotechnol.* **2012**, *7*, 699.
[48] A. S. Pawbake, M. S. Pawar, S. R. Jadkar, D. J. Late, *Nanoscale* **2016**, *8*, 3008.
[49] P. Gao, Y. Y. Zhang, L. P. Wang, S. L. Chen, Y. Huang, X. M. Ma, K. H. Liu, D. P. Yu, *Nano Energy* **2017**, *32*, 302.
[50] A. Sohn, S. Choi, S. A. Han, T. H. Kim, J. H. Kim, Y. Kim, S. W. Kim, *Nano Energy* **2019**, *58*, 811.
[51] B. Radisavljevic, A. Kis, *Nat. Mater.* **2013**, *12*, 815.
[52] J. Zhang, H. Yu, W. Chen, X. Z. Tian, D. H. Liu, M. Cheng, G. B. Xie, W. Yang, R. Yang, X. D. Bai, D. X. Shi, G. Y. Zhang, *ACS Nano* **2014**, *8*, 6024.
[53] K. Kaasbjerg, K. S. Thygesen, K. W. Jacobsen, *Phys. Rev. B* **2012**, *85*, 115317.
[54] M. Hafeez, L. Gan, H. Q. Li, Y. Ma, T. Y. Zhai, *Adv. Funct. Mater.* **2016**, *26*, 4551.